Accelerated Spatially Encoded Spectroscopy of Arbitrarily Shaped Compartments Using Prior Knowledge and Linear Algebraic Modeling

Paul A. Bottomley & Yi Zhang

Johns Hopkins University, Baltimore, MD, USA

Low signal-to-noise ratios (SNR) and long scan times are endemic in spatially localized spectroscopy. While chemical shift imaging (CSI) offers the best SNR efficiency, the minimum scan time is set by the need to acquire a full set of phase-encoding gradients steps (PEs), even if an average spectrum from a multi-voxel compartment would suffice. Moreover, adding voxels to create a compartment-average spectrum post-acquisition sacrifices SNR compared to directly acquiring the spectrum from a correctly sized compartment. Spectroscopy with linear algebraic modeling (SLAM) is a relatively new approach to localization that directly encodes spectra in C arbitrarily prescribed compartments that are segmented from accompanying scout images. SLAM uses a tiny subset ($\geq C$) of the CSI PEs selected from central k-space plus prior knowledge of the compartments, to maximize SNR/volume and greatly reduce scan times. Spectra representing compartment averages are reconstructed by solving a set of C linear simultaneous equations that eliminate unneeded PEs from the standard CSI algorithm. SLAM is further optimized for SNR and compartmental bleed errors, by permitting fractional- instead of integer-stepped gradients. SLAM is amenable to spatial and temporal inhomogeneity corrections, as used routinely in CSI. Combining SLAM with sensitivity encoding (SENSE) techniques from parallel MRI permits replacement of even more of the already-reduced SENSE encoding PEs, for even faster acquisitions. Adoption of the technique in initial cardiac ^{31}P and brain ^{1}H patient studies has demonstrated effective acceleration factors of 4- to 120-fold, SNR efficiency gains of several-fold, and accurate metabolite quantification with respect to reference CSI scans.

Keywords: spectroscopy, localization, chemical shift imaging, SLAM, human studies, reconstruction techniques, pulse sequences

How to cite this article:
eMagRes, 2015, Vol 4: 89–104. DOI 10.1002/9780470034590.emrstm1438

Introduction

Scan time and signal-to-noise ratio (SNR) constitute the main technical impediments to in vivo spatially localized magnetic resonance spectroscopy (MRS) of low-concentration metabolites. Compared to single volume element (voxel) MRS techniques, such as PRESS,[1] STEAM,[2] and ISIS,[3] the standard multi-voxel chemical shift imaging (CSI) method[4] has the advantages of accessing multiple regions simultaneously with higher SNR per unit scan time. However, the clinical application of CSI is limited by the long scan time required for a complete set of phase-encoded acquisitions before any individual spectra can be reconstructed. Often, the acquisition of spectra from multiple spatially resolved voxels is essential for human studies,[5–15] while the massive number of spectra and voxels provided by CSI is over-kill. Spectra from a few, say $C \leq 10$, compartments would suffice; however, the C-fold sacrifice in scan time for single voxel acquisitions compared to CSI may not be tolerable.

In addition, owing to the way that SNR adds in magnetic resonance imaging (MRI) and MRS, there is a significant cost to SNR whenever the CSI voxel size is set smaller than the desired compartment during acquisition.[16,17] This loss cannot be restored by co-adding voxel signals post-acquisition. To illustrate this, consider two CSI experiments[4] wherein voxel volumes V and $V/4$ are encoded with SNR = 20 per unit volume V, in the same total scan time T. As given in Table 1, if V is the ultimate voxel size of interest, the SNR obtained by directly encoding V from the outset is double that of performing the $V/4$ experiment in the same scan time and then co-adding the individual spectra post-acquisition. This result obtains because SNR adds as $\sqrt{n}$ and the noise is independent of the voxel size.[16] Therefore, matching the CSI voxel size to the desired anatomical compartment a priori yields the best SNR per unit scan time.[16]

Extending the same principle to an experiment in which an MRS compartment of interest is directly encoded with CSI gradients, the SNR gain is:

$$g \propto \sqrt{\frac{\text{compartment size}}{\text{CSI voxel size}}} \qquad (1)$$

as compared to co-adding signals from the individual voxels that comprise the compartment in a higher resolution CSI experiment, post-acquisition. The proportionality recognizes

Table 1. Comparison of the SNR for the same ultimate voxel volume (V) and total scan time (T) for two CSI experiments in which V is encoded directly from the outset (#1), vs encoding with resolution $V/4$ and summing the result post-acquisition (#2).

Attribute	Experiment 1	Experiment 2
Voxel size	V	$V/4$
SNR/acquisition	20	5
Averages	4	1
Phase encodes/V	1	4
Scan time	T	T
SNR/voxel/T	40	10
Final SNR/V/T	40	20

the mitigating effects of nonuniform sensitivity and concentrations, and differences in the integrated spatial response function (SRF) of the compartment and its constituent voxels.

Such a g-fold SNR gain could be realized by other MRS localization methods employing phase-encoding gradient steps (PEs) and anatomical compartmentalization, such as SLIM,[18] GSLIM,[19] and SLOOP[20] described elsewhere in this book, if the compartments were prescribed before acquisition (e.g., from scout MRI), and if an appropriate SNR-optimized set of PEs were chosen and applied. Most applications of SLIM, GSLIM, and SLOOP have been limited to retroactively acquired CSI data,[21–26] which precludes realization of this g-fold SNR advantage vs CSI. Undoubtedly, proactive implementation of these MRS methods has been impeded by the difficulty in proactively manipulating the PE gradient sets in commercial MRI scanners. This is likely to change with the advent of compressed sensing MRI techniques,[27] which also requires manipulating the encoding gradients used for MRI.

SLAM, or localized *S*pectroscopy with *L*inear *A*lgebraic *M*odeling,[17,28] is an alternative technique that uses a modified PE gradient set to directly encode, excite, and acquire average spectra from arbitrarily defined anatomical compartments identified from scout MRI, rather than the standard $N\times N$ rectilinear arrays of equally sized CSI voxels. Unlike SLIM, GSLIM, and SLOOP, the gradient set employed for SLAM *is* SNR-optimized, and it permits retrieval of almost all of the missing g-fold SNR advantage vs co-adding the CSI signals to obtain a spectrum from the same compartment. In addition, use of a dramatically reduced set of $\sim C$ PEs permits drastic $(N\times N)/C$-fold reductions in MRS scan times compared to CSI. A minor caveat is that the C prescribed compartments should include all of the MRS signal-generating tissue. Table 2 summarizes differences among the SLIM, GSLIM, SLOOP, and SLAM approaches.

Instead of the standard CSI Fourier transform (FT) algorithm, the SLAM compartment spectra are reconstructed by matrix analysis of a set of C linear simultaneous equations by eliminating unneeded PEs. The $\sim C$ PEs used by SLAM can be chosen from any of the conventional integer-stepped CSI PEs, except that choosing them from the center of k-space results in the highest SNR. Using a strategy of always selecting the PEs from central k-space for a SLAM acquisition results in a gradient set that is fixed only by the number C. This eliminates the requirement that compartments actually be prescribed scanner-side before acquisition: the compartments can be segmented post-acquisition and compartment spectra computed from the highest SNR PE gradient set already acquired. A more advanced version of SLAM, *f*SLAM, uses fractional instead of conventional integer stepped PEs. The fractional PEs are tailored a priori to specific compartment(s), to further maximize SNR and minimize compartmental leakage errors.[17]

SLAM has been implemented in both retroactively acquired MRS data, by dropping all of the high k-space frames of regular CSI acquisitions for testing and validation, and proactively in MRS studies of the human leg, heart, and brain, with 1-D, 2-D, and 3-D (one-dimensional, two-dimensional, and three-dimensional) encoding.[17,28] These studies have demonstrated SNR gains of 30–200% in 1-D ^{31}P studies of the human leg and heart as compared to conventional 1-D CSI for the same net volume and scan time,[17] and acceleration factors from 5 to >100 in 2-D and 3-D applications.[28] SLAM is also amenable to incorporation of all of the conventional ancillary CSI methods for correcting spatial and temporal (i.e., eddy-current) inhomogeneities in the main ($\mathbf{B}_0$) and RF ($\mathbf{B}_1$) fields. In addition, it can also be combined with parallel imaging techniques – SENSE,[29] wherein signals from the individual phased-array detection coils can replace more PEs to achieve even higher acceleration factors.

Localized Spectroscopy with SLAM

The CSI Model

Consider the time-domain (t) signal, $s(k,t)$, acquired in a simple 1-D CSI experiment in the x spatial dimension, with conjugate spatial frequency variable k. $s(k,t)$ is related to the set of CSI spectra in the frequency (f) domain, $\rho(x,f)$, via:

$$s(k,t) = \iint \rho(x,f)\mathrm{e}^{-i2\pi(kx+ft)}\mathrm{d}f\mathrm{d}x \qquad (2)$$

Because the spatial and frequency domains are independent, we also denote the spectrum at x after FT of $s(k,t)$ as $\rho(x)$. For M PEs, $k_1 \ldots k_M$, the discretized version of equation (2) for N time-domain data points is:

$$\begin{bmatrix} s(k_1) \\ s(k_2) \\ \vdots \\ s(k_M) \end{bmatrix}_{M*N} = \begin{bmatrix} \mathrm{e}^{-i2\pi k_1 x_1/M} & \mathrm{e}^{-i2\pi k_1 x_2/M} & \ldots & \mathrm{e}^{-i2\pi k_1 x_M/M} \\ \mathrm{e}^{-i2\pi k_2 x_1/M} & \mathrm{e}^{-i2\pi k_2 x_2/M} & \ldots & \mathrm{e}^{-i2\pi k_2 x_M/M} \\ \vdots & \vdots & \ldots & \vdots \\ \mathrm{e}^{-i2\pi k_M x_1/M} & \mathrm{e}^{-i2\pi k_M x_2/M} & \ldots & \mathrm{e}^{-i2\pi k_M x_M/M} \end{bmatrix}_{M*M} \times \begin{bmatrix} \rho(x_1) \\ \rho(x_2) \\ \vdots \\ \rho(x_M) \end{bmatrix}_{M*N} \qquad (3)$$

Table 2. Comparison among SLIM, GSLIM, SLOOP, SLAM, and fSLAM prior-knowledge-based MRS localization methods.

Property	SLIM	GSLIM	SLOOP	SLAM	fSLAM
Method	CSI PEs and MRI-based segmentation	CSI PEs and MRI-based segmentation	CSI PEs may be optimized to minimize bleed when compartments are nonuniform.	Only the M central *k*-space CSI PEs are used to yield optimum SNR.	Central *k*-space PEs chosen to optimize SNR, errors/ contamination.
Assumption	Every compartment is uniform.	SLIM's nonuniform compartments are addressed with non-Fourier generalized series (GS) basis sets.	Uniform compartments, but gradients adjusted to minimize inter-compartment bleed for nonuniform compartments.	Compartment spectrum is the average of the CSI spectra from each uniform compartment.	Compartment spectrum is the average of the CSI spectra from each uniform compartment, with SNR & errors optimized vs CSI.
Gradient optimization	Not optimized	Not optimized	May be optimized for SNR and inter-compartment bleed.	SNR optimized using minimum number of central *k*-space phase-encodes	Optimized for SNR, inter- & Intra-compartment leakage/errors
Gradient step	Stepped as $\sim n$/FOV, $n = \ldots -2,-1,0,1, 2 \ldots$ (integer)	Stepped as $\sim n$/FOV, $n = \ldots -2,-1,0,1, 2 \ldots$ (integer)	Stepped as $\sim p$/FOV, p integer or non-integer (if optimized)	Stepped as $\sim n$/FOV, with $-M/2 \leq n \leq M/2$, n integer, $C \leq M$	Stepped per optimization. Maximum gradient limited by compartment size.
Reconstruction	Compartment signal computed from the integrated Fourier signal contributions	Same as SLIM, followed by GS constrained modeling to minimize errors	Compartment signal computed from the integrated Fourier signal contributions	Starting from CSI, PEs are eliminated down to C compartments.	Signals acquired with proactively optimized PEs are reconstructed same as SLAM.
Errors	Exact for infinite n. Inter- and intra-compartment errors arise for small n.	Reduces leakage for finite n by applying GS modeling to SLIM result.	Inter-compartment leakage reduced vs SLIM. Intra-compartment nonuniformity errors remain.	Errors increase as the number of phase encodes decrease.	Both inter-compartment bleed and intra-compartment error are suppressed.
In vivo human use (as of 2014)	Applied to retroactive ^{1}H CSI data in human calf.	None	Applied to retroactive ^{31}P CSI data from human heart.	Retroactive and proactive human cardiac ^{31}P and brain ^{1}H MRS done. Quantification validated.	Applied to proactive human cardiac ^{31}P MRS.

Each row of the known signal matrix $\mathbf{S}_{M^*N}$ on the left side of equation (3), and of the unknown spectral matrix $\boldsymbol{\rho}_{M^*N}$ on the right, is an N-point array. The first matrix of exponential terms on the right side is the PE FT operator, **PE**. For simplicity, we write equation (3) as:

$$\mathbf{S}_{M^*N} = \mathbf{PE}_{M^*M} \times \boldsymbol{\rho}_{M^*N} \tag{4}$$

For 1-D CSI, **PE** is simply a discrete Fourier transform (DFT) operator.

Reconstructing Compartment Spectra with SLAM

The goal of the CSI experiment is to reconstruct the M unknown spectra in $\boldsymbol{\rho}_{M^*N}$, from the M known signals (**S**) acquired with M different PEs using equation (4). However, suppose from a scout MRI scan we determine that $\boldsymbol{\rho}$ has just C ($<M$) MRS compartments of interest. If the spatial location and extent of each compartment can be defined, then in theory, only C measurements with C PEs would suffice to solve $\boldsymbol{\rho}$ and reconstruct the C spectra.

For example, consider a four-voxel 1-D CSI experiment. Equation (3) can be written:

$$\begin{bmatrix} e_{11} & e_{12} & e_{13} & e_{14} \\ e_{21} & e_{22} & e_{23} & e_{24} \\ e_{31} & e_{32} & e_{33} & e_{34} \\ e_{41} & e_{42} & e_{43} & e_{44} \end{bmatrix} \times \begin{bmatrix} \rho_1 \\ \rho_2 \\ \rho_3 \\ \rho_4 \end{bmatrix} = \begin{bmatrix} s_1 \\ s_2 \\ s_3 \\ s_4 \end{bmatrix} \tag{5}$$

where $e_{i,j}$ denote the exponential terms. If, based on prior information, the second and third rows of $\boldsymbol{\rho}$ can be considered

identical (i.e., $\rho_2 = \rho_3$), then we need to solve only:

$$\begin{bmatrix} e_{11} & e_{12}+e_{13} & e_{14} \\ e_{21} & e_{22}+e_{23} & e_{24} \\ e_{31} & e_{32}+e_{33} & e_{34} \\ e_{41} & e_{42}+e_{43} & e_{44} \end{bmatrix} \times \begin{bmatrix} \rho_1 \\ \rho_2 \\ \rho_4 \end{bmatrix} = \begin{bmatrix} s_1 \\ s_2 \\ s_3 \\ s_4 \end{bmatrix} \quad (6)$$

Because equation (6) is over-determined, the minimum number of PEs needed to resolve ρ_1, ρ_2, and ρ_4 reduces from 4 to 3. The same procedure allows us to reconstruct C spectra from C homogeneous compartments using only C PEs instead of M steps.

In general, the prior information can be incorporated by introducing a matrix, **b**, formed from an identity matrix in which '−1' elements are inserted to zero-out identical rows in the $\boldsymbol{\rho}$-matrix to leave only one spectrum per compartment. For example, for an eight-voxel 1-D CSI experiment performed on a two-compartment sample in which the first compartment extends from voxels #1–3 and the second extends from voxels #4–8,

$$\mathbf{b} = \begin{bmatrix} 1 & 0 & 0 & 0 & 0 & 0 & 0 & 0 \\ -1 & 1 & 0 & 0 & 0 & 0 & 0 & 0 \\ -1 & 0 & 1 & 0 & 0 & 0 & 0 & 0 \\ 0 & 0 & 0 & 1 & 0 & 0 & 0 & 0 \\ 0 & 0 & 0 & -1 & 1 & 0 & 0 & 0 \\ 0 & 0 & 0 & -1 & 0 & 1 & 0 & 0 \\ 0 & 0 & 0 & -1 & 0 & 0 & 1 & 0 \\ 0 & 0 & 0 & -1 & 0 & 0 & 0 & 1 \end{bmatrix} \quad (7)$$

Here, only the spectra in the compartments corresponding to voxels #1 and #4 are kept after dimensional reduction. The signal is:

$$\mathbf{S}_{M^*N} = \mathbf{PE}_{M^*M} \times \mathbf{b}^{-1}_{M^*M} \times \mathbf{b}_{M^*M} \times \boldsymbol{\rho}_{M^*N} \quad (8)$$

If $M' \geq C$ PEs are predefined and the identical rows are eliminated to reduce the dimension of $\mathbf{b}_{M^*M} \times n_{M^*N}$ from M to C, then equation (8) shrinks to,

$$\mathbf{S}_{M'^*N} = \mathbf{PE}^r_{M'^*C} \times \boldsymbol{\rho}^r_{C^*N} \quad (9)$$

Here, $\boldsymbol{\rho}^r_{C^*N}$ is a submatrix of the C non-eliminated rows of $\mathbf{b}_{M^*M} \times \boldsymbol{\rho}_{M^*N}$; $\mathbf{PE}^r_{M'^*C}$ is a submatrix of $\mathbf{PE}_{M^*M} \times \mathbf{b}^{-1}_{M^*M}$ with C columns that correspond to the C non-eliminated rows; and $\mathbf{S}_{M'^*N}$ is a submatrix of $\mathbf{S}_{M^*N}$ acquired from the sample using the subset of $M' \ll M$ PEs. Solving equation (9) results in a set of spectra that each closely approximate the average spectrum from each compartment.

The SLAM Recipe

The SLAM experiment is thus performed as follows:

1. Acquire an MRI to extract the prior knowledge of the number of compartments ($C \ll M$), and the spatial location and extent of each compartment for SLAM reconstruction.
2. Choose $M' \geq C$ PEs.
3. Apply the chosen M' PEs and acquire the M' signals.
4. Determine the **b** matrix from the spatial position of each compartment identified by MRI.
5. Reduce the dimensions from M to C and compute the C spectra in the $\boldsymbol{\rho}^r$ matrix using:

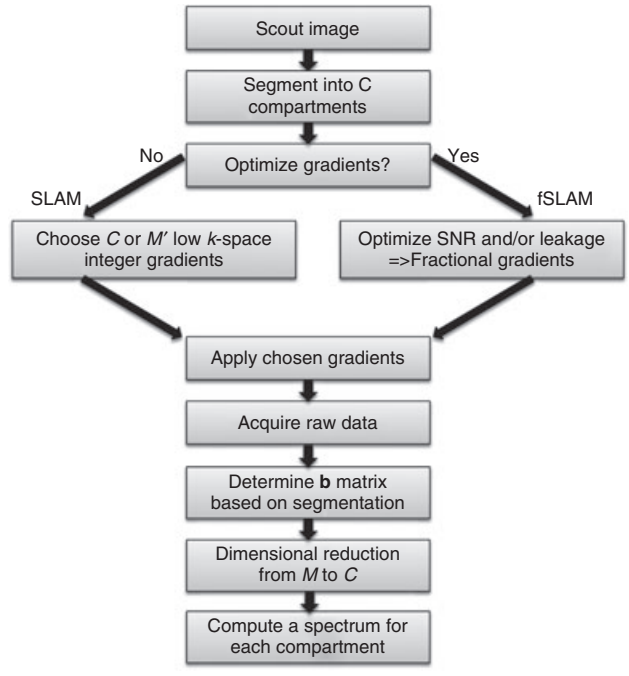

Figure 1. Flow chart depicting implementation of SLAM (left pathway) or fSLAM (right pathway).[17] (Reprinted from J. Magn. Reson., 218, Y. Zhang, R. E. Gabr, M. Schar, R. G. Weiss, and P. A. Bottomley, Highly-accelerated quantitative 2D and 3D localized spectroscopy with linear algebraic modeling (SLAM) and sensitivity encoding, 66–76, Copyright (2012), with permission from Elsevier)

$$\boldsymbol{\rho}^r_{C^*N} = \mathbf{PE}^+_{C^*M'} \times \mathbf{S}_{M'^*N} \quad (10)$$

where '+' denotes either the Moore–Penrose pseudo-inverse when $M' > C$ or the inverse for $M' = C$, of $\mathbf{PE}^r_{M'^*C}$.

Figure 1 presents a block diagram of the reconstruction algorithm.

Because reconstruction of the SLAM compartment spectra simply involves solution of a set of linear simultaneous equations, theoretically, the choice of gradients in Step 2 is arbitrary. However, different choices result in different SNR and condition numbers for the matrix $\mathbf{PE}^r_{M'^*C}$, which affect computational accuracy.[30] Importantly, selecting the M' PEs that lie closest to the center of k-space of the original CSI gradient steps, generally yields the best SNR. Because the CSI steps are discrete and fixed, by applying a rule that all PEs be chosen from central k-space, the set of PEs used in any SLAM experiment is determined entirely by the number M' or C. Furthermore, because C is typically the same for a given study protocol (e.g., C=4 in cardiac studies with chest, heart, and/or adipose and ventricular blood compartments), the same SLAM gradient set can be used for all studies performed with a given protocol. This strategy eliminates the need for scanner-side gradient optimization or image-based gradient prescription before acquisition, while ensuring optimum or near-optimum SNR for each exam.

SLAM with Fractional Gradients (fSLAM)

Choosing the M' PEs need not be limited to the original CSI basis set of M integer (k_i) stepped gradients in equation (3). The M' PEs can instead be chosen to optimize desirable properties of the reconstruction, such as to maximize SNR and/or minimize inter- or intra-compartmental signal contamination or errors. This effectively requires accommodating fractional k's in the CSI equation. The trade-off is that unlike SLAM, fractional SLAM, denoted fSLAM, being tailored to optimize a specific desired compartment(s) does require scanner-side gradient optimization and prescription.

fSLAM with Maximized SNR. In order to maximize the SNR, equation (10) is modified to include noise terms $\boldsymbol{\varepsilon}_{M'*N}$ whose standard deviation (SD) in the time-domain signal is σ:

$$\boldsymbol{\rho}^r_{C*N} + \boldsymbol{\xi}_{C*N} = \mathbf{PE}^+_{C*M'} \times (\mathbf{S}_{M'*N} + \boldsymbol{\varepsilon}_{M'*N}) \qquad (11)$$

where ξ_{C*N} is the noise in the reconstructed spectra. The noise in the time and frequency domains are related via $\boldsymbol{\xi}_{C*N} = \mathbf{PE}^+_{C*M'} \times \boldsymbol{\varepsilon}_{M'*N}$, so the SNR of the spectrum reconstructed from the ith compartment is:

$$\mathrm{SNR}_i = \frac{\boldsymbol{\rho}^r_{C*N}(i)}{\sqrt{\sum_{m=1}^{M'} [|\mathbf{PE}^+_{C*M'}(i,m)|^2 \times \sigma^2]}} \qquad (12)$$

where $\mathbf{PE}^+_{C*M'}(i,m)$ is the element corresponding to the mth signal. To maximize the SNR of the ith spectrum in equation (12), the cost-function

$$\Gamma_i = \sum_{m=1}^{M'} [|\mathbf{PE}^+_{C*M'}(i,m)|^2]/I_{\mathrm{cond}} \qquad (13)$$

is numerically minimized. Here, $I_{\mathrm{cond}} = 1$ when the condition number[30] of $\mathbf{PE}^+_{C*M'}$ is less than a user-defined threshold u, and '0' otherwise, to ensure that the equation system is well conditioned. Minimization of Γ_i, yields the best SNR for the ith compartment of the fSLAM experiment, as well as in the SLAM experiment in the case where $\mathbf{PE}^+_{C*M'}$ is limited to integer gradient steps.

For comparison, the SNR of the CSI experiment is:

$$\mathrm{SNR}^{\mathrm{CSI}}_i = (L_i/M)^{1/2} \cdot \boldsymbol{\rho}^{\mathrm{CSI}}_{C*N}(i)/\sigma \qquad (14)$$

where L_i is the size of the ith compartment with average spectrum $\boldsymbol{\rho}^{\mathrm{CSI}}_{C*N}(i)$. When multiplied by $\sqrt{M/M'}$ to account for scan-time differences, the quotient of equations (12) and (14) approximates equation (1) for fSLAM, as well as for SLAM when the C PEs are chosen from central k-space.[17]

Minimizing Localization Errors with fSLAM. So far, every compartment is assumed homogeneous. However, spectra in the CSI basis set that deviate from the compartmental averages can generate signals that cause errors and/or signal bleed artifacts upon reconstruction. To minimize these errors in an fSLAM experiment using M' PEs, the original $\boldsymbol{\rho}$ matrix in equation (8) is decomposed into average and inhomogeneous parts:

$$\begin{aligned}\mathbf{S}_{M'*N} &= \mathbf{PE}_{M'*M} \times \mathbf{b}^{-1}_{M*M} \times \mathbf{b}_{M*M} \times (\boldsymbol{\rho}^{\mathrm{avg}}_{M*N} + \boldsymbol{\rho}^{\mathrm{inhom}}_{M*N}) \\ &= \mathbf{PE}_{M'*M} \times \mathbf{b}^{-1}_{M*M} \times \mathbf{b}_{M*M} \times \boldsymbol{\rho}^{\mathrm{avg}}_{M*N} + \mathbf{PE}_{M'*M} \times \boldsymbol{\rho}^{\mathrm{inhom}}_{M*N}\end{aligned} \qquad (15)$$

Each row in $\boldsymbol{\rho}^{\mathrm{avg}}_{M*N}$ is now the average spectrum of its compartment, and each row in $\boldsymbol{\rho}^{\mathrm{inhom}}_{M*N}$ is the deviation of the true spectrum from its compartmental average. For example, for a three-voxel compartment comprised of single-point spectra with magnitudes [1.1, 1.0, 0.9], the compartment average spectrum will be '1' and the inhomogeneity part will be [0.1, 0, −0.1].

The solution to equation (15) after dimensional reduction is:

$$\mathbf{PE}^+_{C*M'} \times \mathbf{S}_{M'*N} = \boldsymbol{\rho}^{\mathrm{avg}}_{C*N} + \mathbf{PE}^+_{C*M'} \times \mathbf{PE}_{M'*M} \times \boldsymbol{\rho}^{\mathrm{inhom}}_{M*N} \qquad (16)$$

The first term on the right of equation (16) satisfies the ideal homogeneity assumption for which the SLAM reconstruction is valid. The second term gives rise to localization errors and must be minimized. Because $\boldsymbol{\rho}^{\mathrm{inhom}}_{M*N}$ will be unknown in any SLAM study performed without CSI, a reasonable strategy is to minimize the coefficients of $\mathbf{PE}^l_{C*M} = \mathbf{PE}^+_{C*M'} \times \mathbf{PE}_{M'*M}$. Moreover, because the inhomogeneity terms in the same compartment must sum to zero by definition, their mean can be subtracted. For example, if the three coefficients corresponding to the inhomogeneity [0.1, 0, −0.1] above were [1/2, 1/3, 1/6], they would generate the same errors as coefficients [1/6, 0, −1/6] after subtracting the mean value of 1/3. The sum-of-the-squares of these coefficients is smaller than [1/2, 1/3, 1/6], and is independent of the mean coefficient of each compartment. The new matrix of coefficients that results when the mean is subtracted from $\mathbf{PE}^l_{C*M}(i)$ for each compartment, is denoted $\mathbf{PE}^{ll}_{C*M}(i)$.

Generally, localization errors can arise from both inter-compartmental leakage and intra-compartmental signal inhomogeneity. To minimize the *inter*-compartmental leakage into the ith compartment of the fSLAM experiment, the sum-of-the-squares of the coefficients in $\mathbf{PE}^{ll}_{C*M}(i)$ that derive from outside of the ith compartment, is minimized analogous to SLOOP[20]:

$$\phi_i = \sum_{j \neq i}^{C} \sum_{m \in \mathrm{compartment}\ j}^{M} w_{ij} \times |\mathbf{PE}^{ll}_{C*M}(i,m)|^2 \qquad (17)$$

Here, w_{ij} is the weight of inter-compartment leakage from the jth compartment into the ith compartment. w_{ij} could, for example, be adjusted to accommodate intrinsic differences in metabolite concentrations between compartments.

To minimize errors due to intra-compartment inhomogeneity in the ith compartment of the fSLAM experiment, the sum-of-the-squares of the coefficients from within the ith compartment are minimized similarly:

$$\varphi_i = \sum_{m \in \mathrm{compartment}\ i}^{M} w_{ii} \times |\mathbf{PE}^{ll}_{C*M}(i,m)|^2 \qquad (18)$$

where the w_{ii} weight the intra-compartmental errors.

To perform a numerical optimization that minimizes both the inter- and intra-compartmental errors, the cost-function:

$$\Lambda_i = (\phi_i + \varphi_i)/I_{\text{cond}} \tag{19}$$

is minimized for each of the i compartments.

The fSLAM Recipe

In practice, the fSLAM experiment is performed with the same Steps 1–5 as SLAM (Figure 1) except that the PEs in Step 2 are obtained by minimizing the SNR cost-function in equation (13) and/or the error cost-function in equation (19). The different optimizations will generally produce different PE gradient sets comprised of fractional gradients. To optimize for both maximum SNR and minimum localization error, a weighted sum of the ratio of cost functions for fSLAM, to those for SLAM can suffice: equations (13) and (19) have different scales and cannot just be added. The choice of the weighting will depend on the application and error tolerance.

By optimizing SNR, fSLAM can always achieve higher SNR than standard CSI, independent of the number of PEs ($M' \geq C$) that are chosen. This reflects the fact that fSLAM is free to choose fractional PEs that all fall close to central k-space where SNR is greatest. In addition, adding PEs will further reduce signal bleed as Λ_i is minimized.[17] However, as noted earlier, because $\mathbf{PE}^{ll}_{C^*M}(i)$ is derived from $\mathbf{b}$ and requires prior knowledge of compartment location and size, and because the gradients are not constrained to the integer-stepped CSI gradients, gradient optimization and selection for fSLAM must be performed scanner-side as part of the MRS set-up, in order to determine the optimized set of PEs to apply. In initial studies, scanner-side optimization was performed on a lap-top computer using the simplex method (MATLAB '*fminsearch*', MathWorks, Natick, MA) with threshold $u = 50$ in equations (13) and (19), and all the leakage weighting factors, w_{ij} set to '1' in equations (17) and (18).[17]

Computing Leakage and Localization Errors

Because SLAM produces arbitrarily shaped compartments instead of a regular array of voxels that have a point spread function, its spatial selectivity is more appropriately evaluated by an analysis of the SRF.[22,31] The SRF is both specific to each defined compartment, and is dependent on the other compartments.

Consider for example, a three-compartment 1-D SLAM acquisition from a cardiac phosphorus (^{31}P) study whose true continuous signal distribution $f(x)$ can be decomposed into heart, $f_h(x)$, chest, $f_c(x)$, and 'other', $f_r(x)$ compartments. The 'other' compartment is generally required because any unassigned signal originating from outside of the designated compartments is otherwise distributed into the assigned compartments during reconstruction, potentially contributing 'bleed' errors. The SRF of the heart compartment corresponding to the row $\mathbf{PE}^{+}_{C^*M'}(h)$ is:

$$\text{SRF}_h(x) = \sum_k \mathbf{PE}^{+}_{C^*M'}(h) \cdot \exp(-i2\pi kx) \tag{20}$$

The spectrum from the heart compartment is

$$\begin{aligned}\rho_h &= \int_{\text{FOV}} \text{SRF}_h(x) \cdot f(x)\text{d}x \\ &= \int_{\text{heart}} \text{SRF}_h(x) \cdot f_h(x)\text{d}x + \int_{\text{chest}} \text{SRF}_h(x) \cdot f_c(x)\text{d}x \\ &\quad + \int_{\text{other}} \text{SRF}_h(x) \cdot f_r(x)\text{d}x \end{aligned} \tag{21}$$

The second and third integrals in equation (21) represent leakage from chest, $L_{c\to h}$ and 'other', $L_{r\to h}$ signals into the heart compartment. For the chest compartment, we write $f_c(x)$ as a mean $\overline{f_c}$ plus an inhomogeneity $\Delta f_c(x)$. Then:

$$\begin{aligned} L_{c\to h} &= \int_{\text{chest}} \text{SRF}_h(x) \cdot [\overline{f_c} + \Delta f_c(x)]\text{d}x \\ &= \overline{f_c} \cdot \int_{\text{chest}} \text{SRF}_h(x)\text{d}x + \int_{\text{chest}} \text{SRF}_h(x) \cdot \Delta f_c(x)\text{d}x \\ &\leq \overline{f_c} \cdot \int_{\text{chest}} \text{SRF}_h(x)\text{d}x + \int_{\text{chest}} |\text{SRF}_h(x)| \cdot |\Delta f_c(x)|\text{d}x \\ &\leq \overline{f_c} \cdot \int_{\text{chest}} \text{SRF}_h(x)\text{d}x + \max(|\Delta f_c(x)|) \int_{\text{chest}} |\text{SRF}_h(x)|\text{d}x \end{aligned} \tag{22}$$

The last line of equation (22) is the upper limit of contamination of the heart spectrum by chest signal. The upper limit of leakage from other compartments (e.g., $L_{r\to h}$) can be computed similarly.

It is important to recognize that the signal derives from the *integral* of the SRF over each compartment, which the SLAM reconstruction effectively minimizes – or actually zero's out in the case of homogeneous compartments. However, this integral depends fairly critically on the cancellation of positive and negative variations in the SRF outside of each selected compartment.

In a typical example, a clinical surface coil ^{31}P MRS study of the heart employing a standard 16-step, 1 cm resolution 1-D CSI, might expect signals from three voxels in the chest, and up to four voxels in the heart, as depicted in Figure 2(a). An exemplary four-step 1-D SLAM experiment employing only the central four k-space PEs of the CSI acquisition would realize a fourfold acceleration in the minimum scan time, as compared to 16-step CSI. In computing the SRF_h for a metabolite-of-interest such as phosphocreatine (PCr), $f_c(x)$ must account for the much higher signal intensity in the chest owing to the surface coil's higher sensitivity and higher PCr concentration in the chest compared to the heart. If the signal contamination is computed assuming the chest and heart signals are uniform within their own compartments but with the chest signal four times higher than the heart signal (Figure 2a, black curve), the contaminating signals almost perfectly cancel upon integration of the SRF_h's for SLAM and fSLAM, but not CSI, as given in Table 3. When the signal from the chest compartment is in addition varied by up to 30% peak-to-peak due to the

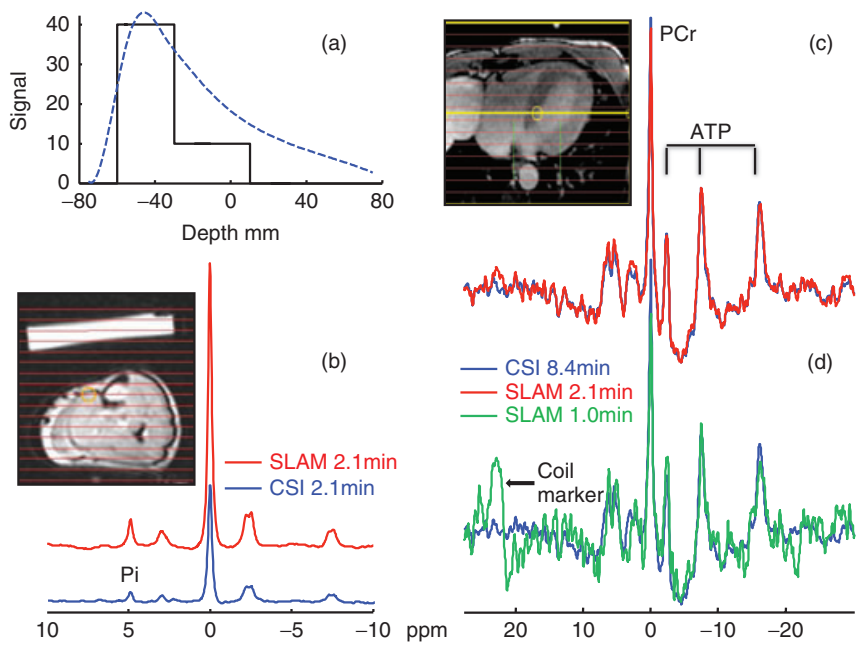

Figure 2. (a) Three-voxel chest, four-voxel heart model used for an SRF analysis of cardiac ^{31}P 1-D CSI data. The chest/heart signal ratio is 4 (black curve; the dashed blue curve depicts a surface coil sensitivity profile). (b) 1-D surface coil ^{31}P spectrum acquired from the same six-voxel volume in the human leg with four-step SLAM (red, top; averaged four times), and with 16-step CSI (blue, lower; one average; Pi =inorganic phosphate), in the same scan time (2.1 min). Locations of the CSI are annotated on the scout image (top left) with the H_3PO_4 disk phantom on top. (c) Surface coil ^{31}P spectra acquired from the same four-voxel volume in a normal human heart (annotated MRI, top left) using 1-D CSI (blue) in 8.4 min, overlaid with a SLAM spectrum (red; ATP =adenosine triphosphate, PCr =phosphocreatine) reconstructed from the four central *k*-space phase-encodes. SLAM assumed a three-compartment model (chest, heart and 'other'). (d) SLAM spectra using just two phase-encodes (green), and a two-compartment model (chest and heart). The effective SLAM acquisition times were 1/4th and 1/8th of CSI. (Adapted from J. Magn. Reson., 218, Y. Zhang, R. E. Gabr, M. Schar, R. G. Weiss, and P. A. Bottomley, Highly-accelerated quantitative 2D and 3D localized spectroscopy with linear algebraic modeling (SLAM) and sensitivity encoding, 66–76, Copyright (2012), with permission from Elsevier)

coil's sensitivity profile (Figure 2a), the upper bound, $L_{c\to h}$, for contamination of the heart compartment by chest muscle PCr rises to 12–14% for fSLAM and SLAM. However, this is still comparable to the 9% seen by the reference 16-step CSI. Meanwhile, a four-step CSI (zero-filled to 16 steps) would be basically unusable (Table 3; 77%).

Inhomogeneity and Segmentation Errors

In the absence of inhomogeneity or noise, computer simulations of the accuracy of SLAM for the three (chest, heart, and 'other') compartment 1-D cardiac ^{31}P MRS model above, produces indistinguishable results from the 16-step CSI acquisition with only the three central *k*-space PEs.[17] Even with the effects of white noise (SNR=20 for the heart component), random inhomogeneity (up to ±15%, or 30% total; Figure 2a) and variable compartment size (chest, 2–3 voxels; heart, 2–6 voxels; separation, 0–1 voxel) included, Monte Carlo analysis shows that the mean error of SLAM compared to regular CSI of the same compartment is <10%.[17]

Monte Carlo simulations of the sensitivity of SLAM to random segmentation errors of between −2 and +2 mm at the edges of either heart or chest compartments, and partial volume errors of ±2 mm, also show that SLAM is either less sensitive or comparable to CSI, as compared to the true spectrum from the compartment.[17] This is important as perfect segmentation is rarely possible in practice, especially in cardiac ^{31}P MRS.

Applications to 1-D ^{31}P MRS with Surface Coil Detection

SLAM and fSLAM have been evaluated in ^{31}P MRS studies of phantoms, the human leg, and the human heart, performed on a 3T Philips Achieva MRI/MRS system to test its suitability for replacing an existing, proven 1-D CSI protocol.[6,8,9,32,33] The 1-D CSI protocol employed 16 integer-stepped PEs ($k = -8, -7, -6, -5, -4, -3, -2, -1, 0, 1, 2, 3, 4, 5, 6, 7$) with 1 cm resolution, and a surface coil detector.[17] The compartment average spectra delivered by SLAM and fSLAM were compared with the sum of CSI spectra from the voxels of the equivalent segmented volumes, post-acquisition. Scanner-side fSLAM optimization required 1–2 min to manually segment the scout MRI, and a few seconds to optimize the gradient set on the lap-top computer.

Figure 2 shows examples of ^{31}P SLAM in the human leg and heart. In the leg study (Figure 2b), a 2.5×15 cm disk phantom containing 300 mM H_3PO_4 was positioned on top of the leg as an additional intense signal source to test contamination. A three-compartment model was assumed. The SLAM experiment employed only the four central CSI *k*-space steps ($k = -2, -1, 0, 1$) repeated four times for the same total scan time as CSI. The SNR of the SLAM spectrum from the leg compartment is twice that of the CSI spectrum obtained by adding the six CSI voxels in the same compartment, and there is negligible signal contamination from the H_3PO_4 phantom (Figure 2b).

Table 3. Integral of SRF_h and upper bound of chest contamination for CSI, SLAM and fSLAM for a three-voxel chest, four-voxel heart model with a chest/heart signal ratio of 4 (Figure 2a).[17]

	16-step CSI	4-step CSI	SLAM	fSLAM
Integral of SRF_h over chest[a]	0.014	0.17	0.005	0.007
Upper bound of $L_{c\to h}$[b]	9%	77%	14%	12%

[a]Computed assuming homogeneous chest and heart signals (Figure 2a, black line).
[b]Computed with ±15% (total 30%) inhomogeneity in the chest signal.

Figure 2(c) shows cardiac spectra from a four-voxel 16-step 1-D CSI heart compartment, along with SLAM spectra acquired with four and two PEs. Signal bleed from adjacent chest skeletal muscle and an embedded coil marker (at ~23 ppm) appears negligible in the four-step experiment, which reproduces the CSI heart spectrum in 1/4th of the scan time. Even with only two steps and a two-compartment model, the SLAM reconstruction yields a good approximation to the CSI reference, but eight times faster (Figure 2d).

The accuracy of quantification with 1-D ^{31}P SLAM was tested by comparing measurements of PCr and (γ-) adenosine triphosphate (ATP) peak areas from 16-step CSI data, with those from SLAM spectra reconstructed using only the central four PEs of the same CSI data. Results from healthy volunteers and patients with cardiomyopathy (Figure 3) showed no significant differences in PCr, ATP, PCr/ATP, or even the total PCr from the chest-plus-heart compartments,[17] despite the effectively fourfold scan-time reduction. As in the leg (Figure 2b), proactive cardiac ^{31}P SLAM and fSLAM spectra demonstrate higher SNR than 16-step CSI acquired from the same volume in the same subject acquired in the same total scan time (Figure 4). The average gain in SNR for cardiac PCr in six healthy subjects was 32–45%.[17] This is consistent with a g-fold gain from equation (1) equivalent to combining two of the 1 cm CSI voxels, even though the reconstruction typically assumed a four-voxel cardiac compartment. This likely reflects the mitigating effect of the declining surface coil sensitivity profile (Figure 2a), and limited 1–2 cm thickness of the anterior myocardium. Signal bleed from the coil marker is reduced either by designating a separate compartment for the coil phantom (Figure 4b), or using fSLAM (Figure 4c).

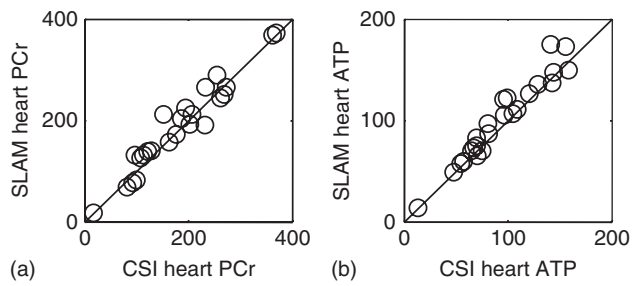

Figure 3. (a, b) Fitting results for PCr and γ-ATP peak areas reconstructed by SLAM from a subset of 4 of the 16 CSI phase encoding steps acquired from cardiac ^{31}P MRS studies of heart patients and healthy subjects, as compared to the CSI measurements.[17] Peak areas were quantified in the cardiac compartment using 'circle fit'[34] (correlation coefficient, $r > 0.97$). (Reprinted from J. Magn. Reson., 218, Y. Zhang, R. E. Gabr, M. Schar, R. G. Weiss, and P. A. Bottomley, Highly-accelerated quantitative 2D and 3D localized spectroscopy with linear algebraic modeling (SLAM) and sensitivity encoding, 66–76, Copyright (2012), with permission from Elsevier)

SLAM and Sensitivity Encoding in Higher Dimensions

This section describes the extension of SLAM to 2-D and 3-D MRS applications, its combination with multiple-receiver sensitivity encoding techniques analogous to the SENSE MRI method used with phased-array detectors,[29,35,36] how to incorporate corrections for spatial and temporal inhomogeneity like those routinely used in clinical MRS, and how to compute the discrete spatial response function (dSRF) of compartments localized by SLAM.

Sensitivity Encoding with the SLAM Model

The number of PEs used by SLAM can be further reduced when additional (phased-array) detectors are available for spatial sensitivity encoding. This is accommodated by rewriting equation (3) more generally as:

$$\mathbf{S}_{M'*N} = \mathbf{E}_{M'*M} \times \boldsymbol{\rho}_{M*N} \tag{23}$$

Here **E** is a combined phase- and sensitivity-encoding operator that incorporates **PE**. $M'=N_c{}^*M_R$ where $N_c \geq 1$ is the number of coil channels used for sensitivity encoding. M_R is the new reduced number of PEs, equal to M/R, where R is SENSE acceleration factor. **E** is constructed by stacking elements comprised of the product of **PE** with the sensitivity encoding matrix, **SE** for each coil element[35]:

$$\mathbf{E} = \begin{bmatrix} \mathbf{PE}_{M_R*M} \times \mathbf{SE}^1_{M*M} \\ \mathbf{PE}_{M_R*M} \times \mathbf{SE}^2_{M*M} \\ \vdots \\ \mathbf{PE}_{M_R*M} \times \mathbf{SE}^{N_c}_{M*M} \end{bmatrix} \tag{24}$$

Here, superscripts 1, 2, …, N_c denote each coil element. For 2-D or 3-D CSI, **PE** is the Kronecker product[37] of double- or triple-serial DFT operators, respectively.

Applying the SLAM theory in section titled 'Reconstructing Compartment Spectra with SLAM' with **PE** replaced by **E** and assuming that the individual CSI spectra in each of the C compartments are identical, yields after dimensional reduction:

$$\mathbf{S}_{M'*N} = \mathbf{E}_{M'*M} \times \mathbf{b}^r_{M*C} \times \boldsymbol{\rho}^r_{C*N} \tag{25}$$

The solution for $\boldsymbol{\rho}^r_{C*N}$ corresponding to the C compartment spectra in the non-eliminated rows of $\boldsymbol{\rho}_{M*N}$ is:

$$\boldsymbol{\rho}^r_{C*N} = (\mathbf{E}_{M'*M} \times \mathbf{b}^r_{M*C})^+ \times \mathbf{S}_{M'*N} \tag{26}$$

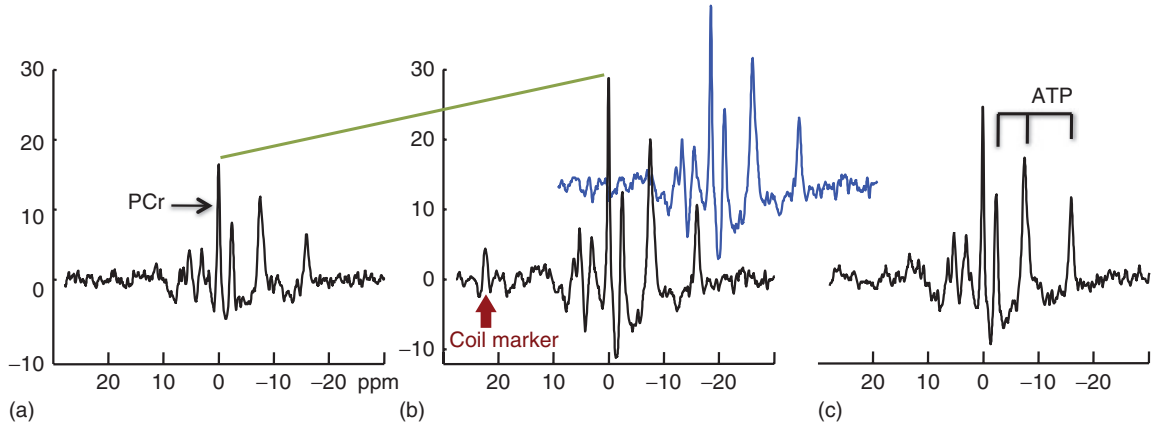

Figure 4. Compartment average cardiac spectra acquired with: (a) 16-step CSI; (b) 4(blue)- and 3(black)-compartment SLAM; and (c) with error-minimized three-compartment fSLAM from the same volunteer. The spectra were all acquired with the same total scan time and total voxel volume, and are normalized to constant noise. CSI used integer PEs (−8 to +7). SLAM used integer PEs of −2, −1, 0, 1 repeated four times. fSLAM used non-integer PEs of −2.13, −0.73, +0.73, +2.13 repeated four times. (Adapted from J. Magn. Reson., 218, Y. Zhang, R. E. Gabr, M. Schar, R. G. Weiss, and P. A. Bottomley, Highly-accelerated quantitative 2D and 3D localized spectroscopy with linear algebraic modeling (SLAM) and sensitivity encoding, 66–76, Copyright (2012), with permission from Elsevier)

with $\mathbf{b}^{r}_{M^*C}$ representing the C columns in $\mathbf{b}^{-1}_{M^*M}$ corresponding to the C non-eliminated rows. Equations (25) and (26) are equivalent to equations (9) and (10) but with sensitivity encoding incorporated. A slightly different algorithm, denoted by asterisks (SLAM* or SENSE SLAM*) is:

$$\boldsymbol{\rho}^{r}_{C^*N} = (\mathbf{b}^{r}_{M^*C})^{+} \times (\mathbf{E}_{M'^*M})^{+} \times \mathbf{S}_{M'^*N} \qquad (27)$$

Both equations (26) and (27) require that $M' \geq C$. Note that with SENSE included, $M'=N_cM/R$ can easily exceed M, making $(\mathbf{E}_{M'^*M})^{+}$ over-determined (e.g., with $N_c = 32$ detector coils and an acceleration factor of $R = 16$). In any case, numeric regularization is recommended, especially where SENSE reconstruction is involved and the SNR is low, as is often the case with MRS. A truncated singular value decomposition (TSVD)[38] method can be used, for example, discarding values below 2% of the maximum to ensure that the condition number $\leq$50,[30] or increasing the level of numeric regularization until the results become stable.

The Discrete Spatial Response Function

With the higher dimensionality of 2-D and 3-D SLAM, and SENSE, as well as the discretization imposed by **SE** in the **E** matrix needed to accommodate the SENSE encoding, it is practical to replace the continuous SRF used for analyzing leakage in section titled 'Computing Leakage and Localization Errors', by a dSRF that treats the spatially discrete CSI spectra as 'ground truth'. The CSI spectra are measurable in practice and can reasonably approximate the various SLAM compartments, whereas, except for phantoms the spatially continuous spectra are generally unknown. For (SENSE) SLAM,

$$\mathbf{dSRF}_{C^*M} = (\mathbf{E}_{M'^*M} \times \mathbf{b}^{r}_{M^*C})^{+} \times \mathbf{E}_{M'^*M} \qquad (28)$$

and for (SENSE) SLAM*,

$$\mathbf{dSRF}_{C^*M} = (\mathbf{b}^{r}_{M^*C})^{+} \times (\mathbf{E}_{M'^*M})^{+} \times \mathbf{E}_{M'^*M} \qquad (29)$$

The contribution to the reconstructed (SENSE) SLAM spectrum for the ith compartment from any specific spatial region can be calculated from these dSRFs via:

$$\boldsymbol{\rho}^{r}_{C^*N}(i,:) = \sum_{j=1}^{M} [\mathbf{dSRF}_{C^*M}(i,j) \times \boldsymbol{\rho}_{M^*N}(j,:)] \qquad (30)$$

where $\boldsymbol{\rho}^{r}_{C^*N}(i,:)$ signifies that only the ith ($1 \leq i \leq C$) row corresponding to the ith compartment is selected from the (SENSE) SLAM spectral matrix, $\boldsymbol{\rho}^{r}_{C^*N}$; $\mathbf{dSRF}_{C^*M}(i,j)$ is the element at the ith row and jth column of $\mathbf{dSRF}_{C^*M}$; j ($1 \leq j \leq M$) is an index for each of all M spatial voxels; and $\boldsymbol{\rho}_{M^*N}(j,:)$ is the jth spectrum in the (SENSE) CSI spectral matrix, $\boldsymbol{\rho}_{M^*N}$.

If the spatial voxels of $\boldsymbol{\rho}_{M^*N}$ in a specific region are grouped to form a user-defined region k, their contribution to the ith SLAM spectrum in the compartment of interest $\boldsymbol{\rho}^{r}_{C^*N}(i,:)$, is:

$$L_{k\to i} = \sum_{j\in \text{region } k} \mathbf{dSRF}_{C^*M}(i,j) \times [\overline{\boldsymbol{\rho}^{k}} + \Delta\boldsymbol{\rho}^{k}_{M^*N}(j,:)] \qquad (31)$$

where $\overline{\boldsymbol{\rho}^{k}}$ is the average (SENSE) CSI spectrum for region k; and $\Delta\boldsymbol{\rho}^{k}_{M^*N}(j,:) = \boldsymbol{\rho}_{M^*N}(j,:) - \overline{\boldsymbol{\rho}^{k}}$ is the deviation of each individual CSI voxel spectrum in the kth region from its regional mean, analogous to equation (21). Then, analogous to equation (22):

$$\begin{aligned} L_{k\to i} &= \overline{\boldsymbol{\rho}^{k}} \times \sum_{j\in \text{region } k} \mathbf{dSRF}_{C^*M}(i,j) \\ &\quad + \sum_{j\in \text{region } k} \mathbf{dSRF}_{C^*M}(i,j) \times \Delta\boldsymbol{\rho}^{k}_{M^*N}(j,:) \\ &\leq \overline{\boldsymbol{\rho}^{k}} \times \sum_{j\in \text{region } k} \mathbf{dSRF}_{C^*M}(i,j) \\ &\quad + \sum_{j\in \text{region } k} |\mathbf{dSRF}_{C^*M}(i,j)| \times |\Delta\boldsymbol{\rho}^{k}_{M^*N}(j,:)| \end{aligned} \qquad (32)$$

Equation (32) relates the SLAM spectrum reconstructed for the *i*th compartment, to the contributions from the mean signal from each region modulated by the dSRF: the inequality sets an upper bound on contributions arising from regional inhomogeneity.

Correcting for Spatial and Temporal Inhomogeneity

Conventional and SENSE CSI spectra are often corrected for spatial and temporal variations in the $\mathbf{B}_0$ and $\mathbf{B}_1$ fields owing to eddy-currents from the gradient pulses used for spatial localization,[39] and/or the use of surface coils.[22] As in CSI, this does require quantification of the spatial and temporal field inhomogeneities. These are accommodated in SLAM by modifying equation (8) to incorporate a diagonal matrix $\mathbf{A}$ comprised of spatially dependent correction factors, such as reciprocals of the receiver coil sensitivity profile or conjugates of the phase variation at each voxel[39,40]:

$$\mathbf{S}_{M'^*N} = \mathbf{E}_{M'^*M} \times \mathbf{A}^{-1}_{M^*M} \times \mathbf{b}^{-1}_{M^*M} \times \mathbf{b}_{M^*M} \times \mathbf{A}_{M^*M} \times \boldsymbol{\rho}_{M^*N} \quad (33)$$

The corrected reconstruction for (SENSE) SLAM and (SENSE) SLAM* are then, respectively:

$$\boldsymbol{\rho}^r_{C^*N} = (\mathbf{E}_{M'^*M} \times \mathbf{A}^{-1}_{M^*M} \times \mathbf{b}^r_{M^*C})^+ \times \mathbf{S}_{M'^*N} \quad (34)$$

$$\text{and } \boldsymbol{\rho}^r_{C^*N} = (\mathbf{b}^r_{M^*C})^+ \times \mathbf{A}_{M^*M} \times (\mathbf{E}_{M'^*M})^+ \times \mathbf{S}_{M'^*N} \quad (35)$$

Temporal corrections are applied by repeating the reconstruction of equations (33–35) at each time point.

Summary of SENSE SLAM Implementation

The SENSE SLAM experimental protocol is similar to SLAM (see section titled 'The SLAM Recipe'):

I. Acquire MRI for segmenting compartments, and mapping detector coil sensitivity for SENSE;
II. Apply a subset of $M_R \geq C/N_c$ PEs selected from the central *k*-space of a regular CSI sequence or defined by fSLAM (see section titled 'Reconstructing Compartment Spectra with SLAM'), and acquire the MRS data;
III. Register the regular CSI grid onto the corresponding MRI;
IV. Segment the CSI voxels into the C desired anatomical compartments based on the MRI;
V. Reconstruct the compartmental spectra using equation (26) or (27).

An Exemplary Application: Brain ^{1}H MRS

SENSE SLAM(*) Validation in Tumor Studies

SENSE SLAM and SLAM* have been evaluated on a *Philips* 3T MRI scanner using MRI and ^{1}H SENSE CSI MRS data for Ref. 28. The CSI data were acquired from patients with brain tumors using a commercial 32-element SENSE head coil, and a standard multi-slice 2-D spin-echo MRS protocol employing an R =sixfold SENSE acceleration factor. The latter reduced the number of CSI PEs from 33×27=891 rectilinear *k*-space steps, to 11×14=154 steps. This was further reduced to 120 steps, by omitting the corners of *k*-space as shown in Figure 5(a). Peripheral lipids in the scalp were suppressed by eight outer-volume selective suppression slabs that employed dual-band water-lipid-suppression,[41] and an additional 27 CSI PEs were acquired without suppression to provide measures enabling inhomogeneity and eddy-current compensation.[39] This resulted in a total scan time of 6.2 min for three 13 mm transaxial sections with 7×7 mm^2 in-plane resolution for the standard CSI study.[28]

SENSE SLAM and SLAM* reconstruction were performed using 1/5th of the central *k*-space data from the CSI study (Figure 5b), for a net acceleration of 36-fold compared to the original 891-step CSI.[28] An extreme case with $R = 120$ was also evaluated. This was achieved by spatially encoding entirely using SENSE, with only a single central zero-gradient PE acquisition (Figure 5c). Five compartments (#1 = tumor; #2 = contralateral brain; #3 = 'rest of the brain', excluding the first two compartments; #4 = the scalp; and #5 = background) were segmented by overlaying the standard CSI grids on the MRIs. The segmentation included any gridded voxel with a volume intersecting a compartment by 50% or more. Reconstruction was done off-line on a laptop computer. Quantitative comparisons of the $R = 36$ reconstructions with CSI were performed on compartment-averaged brain metabolite areas (choline, Cho); total creatine, CR; and *N*-acetylaspartate, NAA).

Figure 6 shows compartment spectra from SENSE SLAM, SENSE SLAM*, and SENSE CSI for a patient with a large

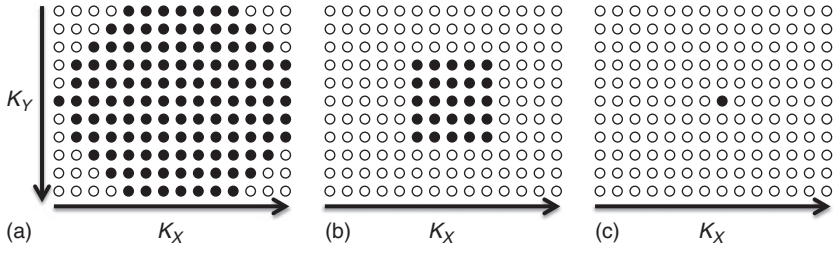

Figure 5. Acquisition schemes depicting *k*-space sampling (filled circles) for: (a) 11×14 SENSE CSI with corners omitted (120 steps); (b) SENSE SLAM(*) acquisitions with a further fivefold acceleration factor (25 steps total); and (c) SENSE SLAM* with 120-fold (one-step total) acceleration.[28] (Reprinted from J. Magn. Reson., 237, Y. Zhang, R. E. Gabr, J. Zhou, R. G. Weiss, and P. A. Bottomley, Magnetic resonance Spectroscopy with Linear Algebraic Modeling (SLAM) for higher speed and sensitivity, 125–138, Copyright (2013), with permission from Elsevier)

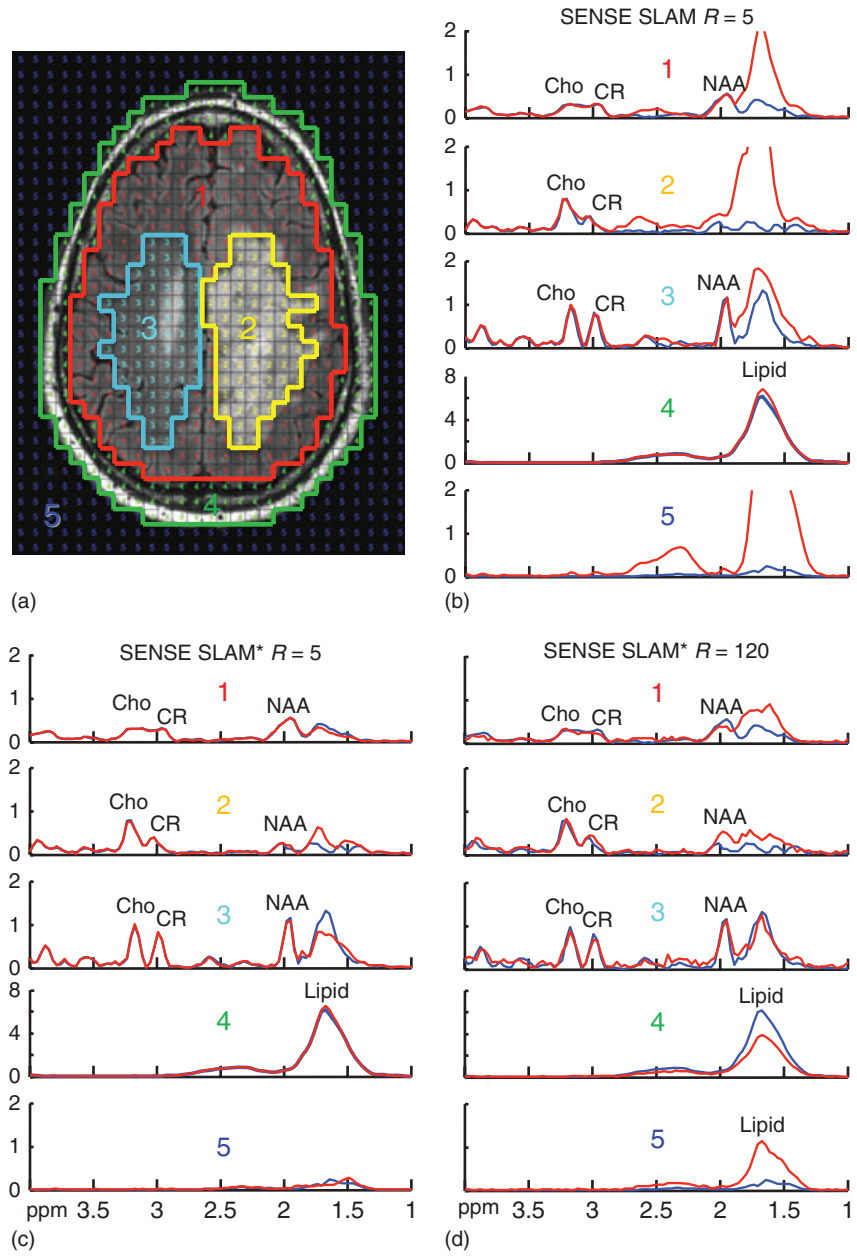

Figure 6. (a) MRI showing segmentation of five compartments in a patient with a brain tumor (#1='rest of the brain'; #2=tumor, glioblastoma; #3=contralateral brain; #4=scalp; #5=background). Spectra (b–d) are from the corresponding compartments (#1–#5) with SENSE CSI spectra depicted in blue for comparison.[28] The (b) SENSE SLAM spectra and (c) SENSE SLAM* spectra, overlaid in red, were reconstructed using 1/5th of the SENSE CSI data, for an effective acceleration factor of $R = 5$ compared to SENSE CSI. The SENSE SLAM* spectra in (d), were reconstructed with $R = 120$.[28] (Adapted from J. Magn. Reson., 237, Y. Zhang, R. E. Gabr, J. Zhou, R. G. Weiss, and P. A. Bottomley, Magnetic resonance Spectroscopy with Linear Algebraic Modeling (SLAM) for higher speed and sensitivity, 125–138, Copyright (2013), with permission from Elsevier)

glioblastoma.[28] The SENSE SLAM and SLAM* spectra (red) are effectively five times (Figure 6b and c) and 120 times faster (Figure 6d) than the SENSE CSI data (blue), respectively. With SENSE, the SLAM* algorithm (equation 27; Figure 6c) outperforms the SLAM algorithm (equation 26; Figure 6b), in the ~1.7 ppm lipid region where strong, broad lipid peaks tend to corrupt the NAA peaks, while SENSE SLAM* spectra (Figure 6c) are relatively unaffected by the lipid peaks. Substantially less spatial leakage is also evident in the background compartment (#5) of SENSE SLAM* as compared to SENSE SLAM. On the other hand, without SENSE using the head coil as a conventional quadrature receiver, the two algorithms appear to perform comparably.[28]

In the extreme case with only the single zero-gradient acquisition, SENSE SLAM* produced reasonably good spectra (Figure 6d) whose tumor compartment (#2), maintains 23% of the SNR of the original SENSE CSI.[28] After correcting for the over two-orders-of-magnitude speed-up in acquisition time,

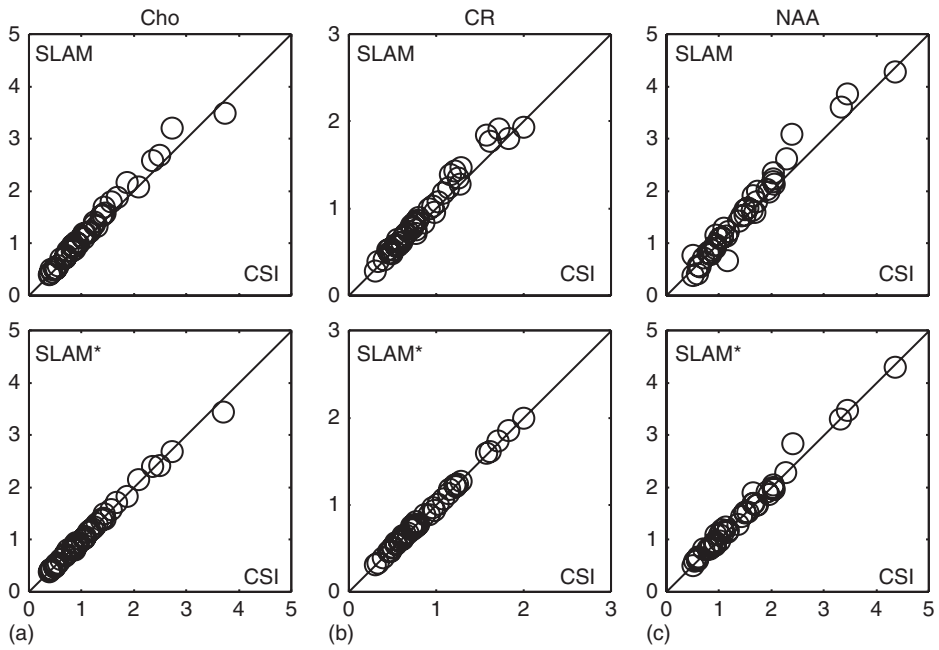

Figure 7. Comparison of SLAM (top row) and SLAM* (bottom row) metabolite measurements reconstructed from 1/6th of the 2-D CSI data acquired from 16 patients, for an effective acceleration factor of $R = 6$. The (a) Cho, (b) CR, and (c) NAA peak areas quantified in tumor, contralateral brain and 'rest of the brain' compartments, are compared with the CSI results from the same compartments (horizontal axis; correlation coefficient $r \geq 0.98$ for all cases).[28] (Adapted from J. Magn. Reson., 237, Y. Zhang, R. E. Gabr, J. Zhou, R. G. Weiss, and P. A. Bottomley, Magnetic resonance Spectroscopy with Linear Algebraic Modeling (SLAM) for higher speed and sensitivity, 125–138, Copyright (2013), with permission from Elsevier)

the SNR per unit volume per unit time is about three times higher than the SENSE CSI data. Importantly, the high Cho/CR characteristic of the tumor is preserved in both SLAM* and SLAM tumor spectra (#2).

Figure 7 shows that pooled Cho, CR, and NAA peak areas quantified in SLAM and SLAM* spectra from the tumor, contralateral and 'rest of the brain' compartments in 16 patient MRS studies, are in quantitative agreement with CSI measurements from the same compartments. The ratios of SLAM to CSI levels for NAA, Cho and CR, were without significant bias, and had SDs of 15, 6, and 6.7% for SLAM, and 6, 3, and 2% for SLAM*, perhaps reflecting a generally higher lipid contamination of NAA.[28]

Implementation of SENSE SLAM* in a proactive study that included eddy-current correction is exemplified in Figure 8. The acceleration factor is R=5 vs an accompanying reference SENSE CSI. The eddy-current correction utilized the 27 PEs acquired with the CSI scan for this purpose. These were zero-filled to the 154-step SENSE CSI grid (Figure 5a), and the spatial and time-dependent phases interpolated across the sample volume,[39] correcting for any phase jumps.[40] In Figure 8(b), the proactive (red) SENSE SLAM*, the accompanying SENSE CSI (blue), and a set of SENSE SLAM* spectra (green) computed from the CSI data, are all coincident. Metabolite measurements with and without eddy-current correction did not differ significantly from CSI in a further eight brain tumor studies. The compartment average SENSE SLAM(*) spectra in these subjects were again insensitive to errors in segmentation compared to reference SENSE CSI from the same mal-adjusted compartments,[28] as was noted for the 1-D case (see section titled 'Inhomogeneity and Segmentation Errors').

The dSRF for SLAM(*) and SENSE SLAM(*) in Practice

In order to quantify the contamination of (SENSE) SLAM(*) spectra by extra-compartmental signals, the dSRF of each specific compartment must be calculated from equations (28)–(32) and then integrated. This is exemplified here for the brain tumor compartment (#1) from Figure 8, which was acquired with the 32-element SENSE coil and R=6 vs SENSE CSI (25 vs 154 PEs; Figure 5b). The dSRF was calculated assuming the five compartments indicated (Figure 9a), both without (TSVD threshold =0%) and with (TSVD threshold =2%) numeric regularization.[28]

The dSRF of SENSE SLAM* obtained from equation (29) without numeric regularization (Figure 9b) is in theory perfect in the tumor compartment, because the combination of 25 PEs plus 32 separate acquisition channels creates $M' = 25 \times 32 = 800$ known k-space signals. Although there are $M = 33 \times 27 = 891$ unknown image-space signals, application of the sensitivity mask during SENSE reconstruction[29] effectively reduces the number of unknowns to <800 so that $(\mathbf{E}_{M'*M})^{+}$ is over-determined. With numeric regularization (TSVD threshold =2%), which is typically needed for matrix inversion when SNR is low, the dSRF is broadened by an amount equivalent to ~20% in each direction compared to Figure 9(b), but it still remains spatially well constrained (Figure 9c). Edge definition improves as the TSVD threshold is reduced.

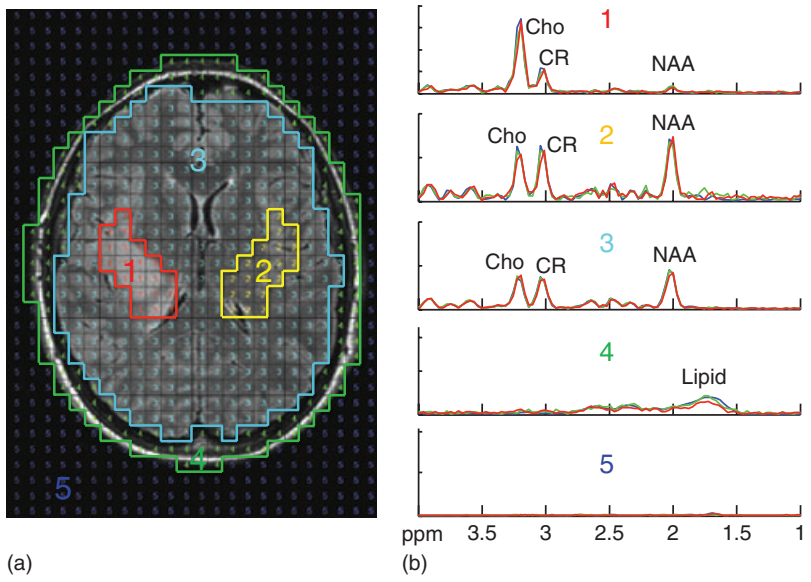

Figure 8. SENSE CSI and SLAM* ^{1}H spectra from a brain tumor patient with eddy-current corrections. The MRI (a) depicts a five-compartment segmentation of a patient with a brain (#1=tumor; #2=contralateral brain; #3='rest of the brain'; #4=scalp; #5=background). (b) The corresponding spectra (#1–#5) are corrected for eddy-currents. SENSE CSI spectra are depicted in blue. Proactively acquired SENSE SLAM* spectra are shown in red with R=5. Retroactive SENSE SLAM* spectra reconstructed from 1/5th of the CSI data set are shown in green. (Adapted from J. Magn. Reson., 237, Y. Zhang, R. E. Gabr, J. Zhou, R. G. Weiss, and P. A. Bottomley, Magnetic resonance Spectroscopy with Linear Algebraic Modeling (SLAM) for higher speed and sensitivity, 125–138, Copyright (2013), with permission from Elsevier).

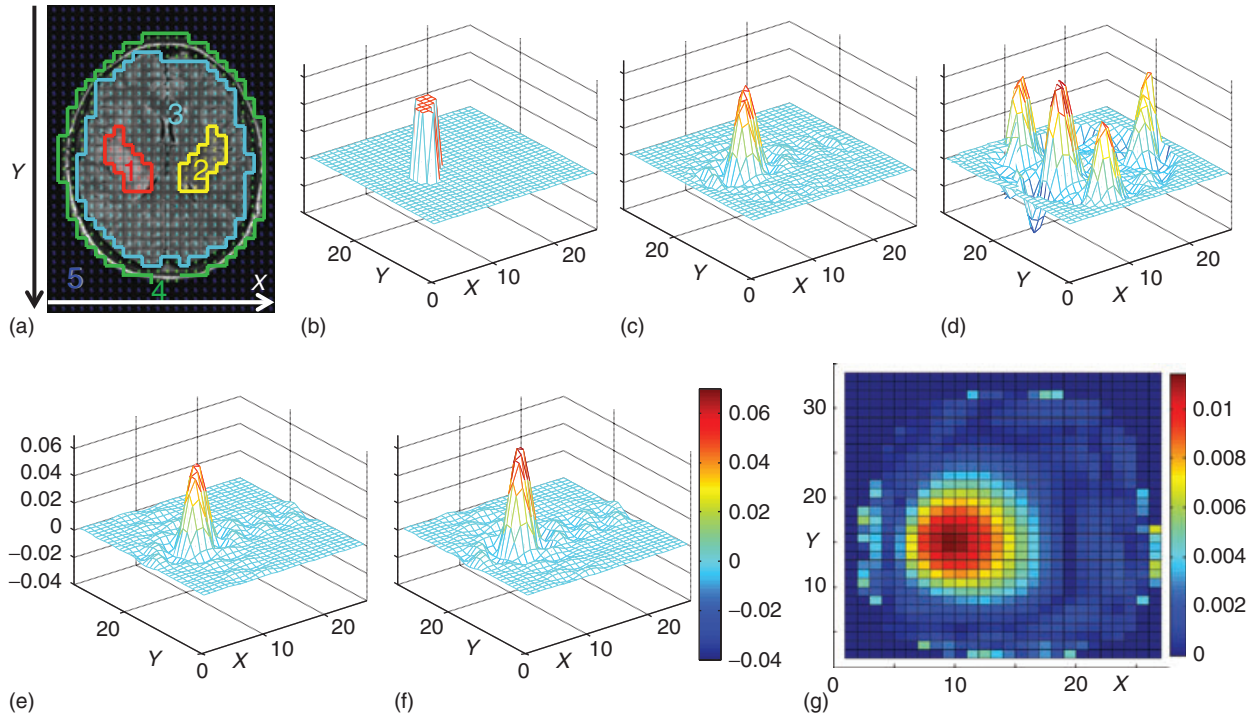

Figure 9. (a) Image of the segmented brain tumor from Figure 8 (compartment #1, red). (b) The real part of the computed tumor dSRF for SENSE SLAM* (R=6 vs SENSE CSI) reconstructed without numeric regularization; and (c) with numeric regularization (TSVD threshold ≤2% of the maximum). (d) The dSRF for SENSE SLAM (R=6 vs SENSE CSI). (e) The dSRFs for SLAM* and for (f) SLAM, both with R=6 vs CSI. (g) The computed dSRF for compartment #3 in the extreme case of a single phase-encode in Figure 6 (intensity scale is arbitrary). (Adapted from J. Magn. Reson., 237, Y. Zhang, R. E. Gabr, J. Zhou, R. G. Weiss, and P. A. Bottomley, Magnetic resonance Spectroscopy with Linear Algebraic Modeling (SLAM) for higher speed and sensitivity, 125–138, Copyright (2013), with permission from Elsevier).

The dSRF of SENSE SLAM obtained from equation (28) on the other hand, is expansive, exhibiting both positive and negative lobes (Figure 9d). Even so, the integral of the dSRF outside the tumor compartment is in fact zero. The SENSE SLAM reconstruction always forces the dSRF integral to zero over the other compartments, facilitated by the spatially oscillating dSRF lobes as noted earlier (see section titled 'Computing Leakage and Localization Errors'; Ref. 17). When these lobes fall in areas that contain strong signal sources, incomplete cancellation can contribute signal contamination, including peripheral lipid signals evident in Figure 6(b). SLAM* does not force the summed dSRF to zero, but does reduce the integral of the magnitude of the dSRF, |dSRF|, thereby reducing the lipid contamination seen in Figure 6(c), for example.

Without the SENSE reconstruction, the dSRF of SLAM* (Figure 9e) and SLAM (Figure 9f), computed with 1/6th of the CSI PEs, are very similar to each other and to the numerically regularized SENSE SLAM* (Figure 9c). Note that while numeric regularization affects the dSRF of SENSE SLAM*, it barely alters that of SLAM, SENSE SLAM or SLAM*.

Finally, Figure 9(g) depicts the dSRF in the extreme case of 120-fold accelerated SENSE SLAM* for compartment #3 of Figure 6(d).[28] Here, with only the single central *k*-space signal, MRS localization is entirely due to the individual SENSE coil inhomogeneity and prior knowledge. Accordingly, there is some signal leakage at the periphery in regions of high sensitivity close to the coils.

Discussion

Summary and Context vs Other Approaches

Single-voxel 3-D MRS localization methods such as PRESS,[1] STEAM,[2] or ISIS[3] are useful for studying single, rectangular-shaped compartments, but do not provide optimum SNR efficiency for studying multiple or arbitrarily shaped compartments. Moreover, their dependence on spatially selective T_1- and T_2-based pulse sequences can introduce relaxation effects that complicate quantification. CSI on the other hand, is a simple pulse-acquire experiment that collects all-of-the-signal from all-of-the-sample, all-of-the-time for maximum SNR efficiency, but is limited by the minimum scan time required to encode the entire sensitive volume, especially with large array sizes. This means that the SNR gained from improved detector technology, higher $\mathbf{B}_0$ magnetic field strengths and the like, is ultimately of limited value in reducing CSI scan times. In addition, CSI's spatial resolution is usually set by the geometry of the tissues that must be distinguished, which often compromises the ability to match voxel size with a desired compartment in order to maximize SNR.[16]

The SLAM method exploits differences in volume sizes between desired MRS compartments and the CSI resolution to realize SNR gains arising from the proportionality of equation (1). Basically, SLAM directly encodes the compartments of interest using only the PEs that have the highest SNR plus the prior MRI-based knowledge of the location and size of the compartments. Moreover, if the 'center of *k*-space' strategy is chosen (vs fSLAM), apart from a scout MRI, the only prior knowledge actually needed to start a SLAM study, is the number of compartments, *C*, which is typically the same for a given application.

SLAM reconstruction involves solving a set of *C* linear simultaneous equations by eliminating unneeded PEs from the standard CSI algorithm, which are therefore not acquired. The resulting set of spectra are at best, equal to the spectra that would have obtained from averaging the individual voxels that comprise each compartment of a regular CSI acquisition, of which the SLAM PEs represent a subset. Indeed, in retroactive and proactive ^{31}P cardiac and ^{1}H brain studies of patients, SLAM can deliver metabolite measures that are quantitatively comparable to results obtained by averaging CSI spectra from the corresponding compartments, and provide many-fold reductions in minimum scan times. Moreover, because the SNR lost by cutting the scan time ($\sim\sqrt{}$[scan time]), is offset in part by the SNR gained by matching the compartment and voxel volumes ($\sim\sqrt{}$[compartment/voxel]), this reduction in minimum scan time enables faster MRS acquisitions at a significantly mitigated cost to the final MRS SNR.

Inter-compartmental signal contamination of SLAM spectra increases with the inhomogeneity of the signal distribution, the intensity of signals in adjacent compartments, and when segmentation omits real signal sources. Such errors can arise from intrinsic variations in tissue metabolite concentrations (e.g., chest vs cardiac muscle in ^{31}P spectra, or scalp lipids in ^{1}H brain spectra) or detector coil sensitivity, which can also be problematic for conventional CSI. For testing, it is a useful feature of SLAM that it can be performed retroactively on raw CSI data that are accompanied by scout MRIs, simply by applying the algorithm to a subset of the central *k*-space frames. The retroactive SLAM spectra can then be compared with the summed CSI from the same-sized compartments for validation, as exemplified above (e.g., Figures 2, 3, 6–8).

fSLAM extends SLAM by removing the limitation that PEs be selected from the set of integer-stepped CSI gradients. The fSLAM gradients are adjusted to minimize leakage or errors due to inhomogeneity and/or maximize SNR. Maximizing SNR alone will typically result in a cluster of PEs at the center of *k*-space that generate potentially unacceptable bleed errors, while only minimizing the compartmental errors yields reasonable results, albeit with a small reduction in SNR (Figure 4c vs b). In addition, note that the SRF is not global but specific to the anatomical model. Inter- and intra-compartmental leakage occurs only when the integral over the entire compartment is nonzero for example, due to the presence of significant intra-compartmental heterogeneity. The segmentation in SLAM ensures that the integral of the SRF vanishes over other compartments, while fSLAM minimizes the effect of heterogeneity within the compartment of interest as well.

Extension to 2-D, 3-D, and SENSE

Multi-receiver SENSE is now state-of-the-art in MRI, and is often implemented with regular ^{1}H CSI as well, where it already provides significant reductions in MRS scan times for CSI. As discussed earlier, SLAM too can incorporate conventional SENSE calibration. Moreover, signals from the individual receiver channels used for SENSE encoding can be used in lieu of the SLAM PEs to further reduce the already-limited PE

gradient set. The upshot is significant additional scan-time accelerations, beyond those provided by SENSE CSI alone. The extreme example is the 120-fold acceleration achieved by replacing *all PEs but a single central k-space* acquisition, with the SENSE inputs from a 32-channel head coil (Figure 6d; Ref. 28). The fidelity of such extreme accelerations will depend on the localization properties of the SENSE coils, and may not work well for other segmentations, data, or applications. Nevertheless, in many cases adding SENSE results in a reconstruction that is many-fold over-determined for the number of compartments being solved. With SENSE, the SLAM* reconstruction algorithm, equation (27), appears better at reducing errors owing to the effects of signal heterogeneity owing to its more spatially confined dSRF compared to equation (26), and may be preferred. Although the integral of the dSRF computed with equation (26) is forced to zero outside a desired compartment, incomplete cancellation of intense extra-compartmental signals such as scalp lipids close to the SENSE coils (Figure 6), can exacerbate bleed artifacts.

While the extension of SLAM to 2-D and 3-D CSI with acceleration factors of up to 120-fold is dramatic (Figure 6d), much lower acceleration factors of say ~fivefold (Figures 4, 6, 8) can represent meaningful, if not enabling, scan-time advantages. Examples include: (i) the reduction of a barely tenable 39 min ^{31}P human cardiac 3-D CSI cardiac scan to just 5$^1/_2$ min – short enough perhaps, to include ^{31}P MRS in a complete functional cardiac MRI exam and (ii) a 3-D ^{1}H MRS of a brain tumor patient performed in 1.5 min with SENSE SLAM* that was otherwise precluded from a SENSE CSI scan by scan time.[28] However, even if the time-saving were not needed, averaging SLAM acquisitions for the same scan time as CSI still deliver significant SNR benefits compared to a compartmental-average CSI spectrum (e.g., Figure 2b).

Conclusion

The SLAM methodology generates localized spectra comparable to the average of equivalent CSI compartments but with potentially huge scan-time reductions, significant SNR gains, and manageable bleed artifacts. It can be used in conjunction with existing MRS tools commonly used in CSI to compensate for field inhomogeneities and eddy-currents, as well as with SENSE to yield scan-time reductions way beyond those already provided by SENSE CSI. These efficiency advantages may be useful for reducing MRS scan times in patient MRS studies involving global disease such as cardiomyopathies,[6,8,9,24,25,32] large lesions, or where single voxel methods are limited by relaxation, motion, or other considerations.[33] The reductions in minimum scan time compared to CSI may also offer a practical means of translating the higher SNR afforded by increases in magnetic field strength and other detector technologies, into faster MRS. The main drawback of SLAM technology at present is that, it is not generally available as a packaged MRS tool on clinical MRI machines. Hopefully, this can change.

Acknowledgments

Supported in part by AHA grant 13GRNT17050100, NIH grant R01EB007829, and the Russell H Morgan Professorship of the Johns Hopkins University Dept of Radiology.

Biographical Sketches

Paul A. Bottomley, BSc(Hon.), 1975, PhD, 1978, Physics, University of Nottingham, UK. Research Associate, Johns Hopkins University, Baltimore, 1978–1980. Physicist, G. E. Research and Development Center, 1980–1994. Currently Russell H Morgan Professor and Director of the Division of MR Research, of the Russell H Morgan Department of Radiology and Radiological Sciences, Johns Hopkins University. Fellow and Gold Medal recipient of the Society of Magnetic Resonance in Medicine, 1989; Coolidge Fellowship and medal, G.E. Company, 1990; Gold, Silver, and Bronze patent medals; 39 issued patents, about 180 peer-reviewed papers, 21 book chapters, 13 editorials, and over 225 published abstracts. Research specialties: in vivo NMR, MRI, tissue relaxation times, localized NMR spectroscopy, human cardiac NMR spectroscopy, interventional MRI, MRI safety.

Yi Zhang, BSc 2009 (Zhejiang University), PhD, 2014, Electrical and Computer Engineering, Johns Hopkins University, USA. Currently post-doctoral fellow, Division of MR Research, Department of Radiology and Radiological Sciences, Johns Hopkins University. Trainee member, International Society for Magnetic Resonance in Medicine (ISMRM), and the Radiological Society of North America. 2012 and 2013 ISMRM Magna Cum Laude Merit awardee; four peer-reviewed papers, eight published conference abstracts, and two patent applications. Research interests include MR spectroscopy, chemical exchange saturation transfer imaging, and image reconstruction and processing.

Related Articles

Spatial Localization Techniques for Human MRS CSI and SENSE CSI; Encoding and decoding with prior knowledge: From SLIM to SPICE; SLOOP and its Modifications; High-speed MRS with PEPSI and spiral MRS; Localized MRS to single voxels with MRI gradients

References

1. P. A. Bottomley, *Ann. N.Y. Acad. Sci.*, 1987, **508**, 333.
2. J. Frahm, K. D. Merboldt, and W. Hanicke, *J. Magn. Reson.*, 1987, **72**, 502.
3. R. Ordidge, A. Connelly, and J. Lohman, *J. Magn. Reson.*, 1986, **66**, 283.
4. T. R. Brown, B. M. Kincaid, and K. Ugurbil, *Proc. Natl. Acad. Sci. U.S.A.*, 1982, **79**, 3523.
5. C. J. Hardy, R. G. Weiss, P. A. Bottomley, and G. Gerstenblith, *Am. Heart J.*, 1991, **122**, 795.
6. R. G. Weiss, P. A. Bottomley, C. J. Hardy, and G. Gerstenblith, *N. Engl. J. Med.*, 1990, **323**, 1593.
7. P. A. Bottomley and R. G. Weiss, *Lancet*, 1998, **351**, 714.
8. R. G. Weiss, G. Gerstenblith, and P. A. Bottomley, *Proc. Natl. Acad. Sci. U.S.A.*, 2005, **102**, 808.
9. C. S. Smith, P. A. Bottomley, S. P. Schulman, G. Gerstenblith, and R. G. Weiss, *Circulation*, 2006, **114**, 1151.
10. J. Kurhanewicz, D. B. Vigneron, H. Hricak, P. Narayan, P. Carroll, and S. J. Nelson, *Radiology*, 1996, **198**, 795.
11. S. J. Nelson, D. B. Vigneron, and W. P. Dillon, *NMR Biomed.*, 1999, **12**, 123.

12. J. Scheidler, H. Hricak, D. B. Vigneron, K. Y. Kyle, D. L. Sokolov, L. R. Huang, C. J. Zaloudek, S. J. Nelson, P. R. Carroll, and J. Kurhanewicz, *Radiology*, 1999, **213**, 473.
13. C. Dowling, A. W. Bollen, S. M. Noworolski, M. W. McDermott, N. M. Barbaro, M. R. Day, R. G. Henry, S. M. Chang, W. P. Dillon, and S. J. Nelson, *Am. J. Neuroradiol.*, 2001, **22**, 604.
14. P. B. Barker, J. H. Gillard, P. Van Zijl, B. J. Soher, D. F. Hanley, A. M. Agildere, S. M. Oppenheimer, and R. N. Bryan, *Radiology*, 1994, **192**, 723.
15. P. B. Barker and D. D. Lin, *Prog. NMR Spectrosc.*, 2006, **49**, 99.
16. P. A. Bottomley and C. J. Hardy, *Philos. Trans. R. Soc. London, Ser. A*, 1990, **333**, 531.
17. Y. Zhang, R. E. Gabr, M. Schar, R. G. Weiss, and P. A. Bottomley, *J. Magn. Reson.*, 2012, **218**, 66.
18. X. Hu, D. N. Levin, P. C. Lauterbur, and T. Spraggins, *Magn. Reson. Med.*, 1988, **8**, 314.
19. Z. P. Liang and P. C. Lauterbur, *IEEE Trans. Med. Imaging*, 1991, **10**, 132.
20. M.von Kienlin and R. Mejia, *J. Magn. Reson.*, 1991, **94**, 268.
21. Z. Dong and J. H. Hwang, *Magn. Reson. Med.*, 2006, **55**, 1447.
22. R. Loffler, R. Sauter, H. Kolem, A. Haase, and M.von Kienlin, *J. Magn. Reson.*, 1998, **134**, 287.
23. M. Meininger, W. Landschütz, M. Beer, T. Seyfarth, M. Horn, T. Pabst, A. Haase, D. Hahn, S. Neubauer, and M.von Kienlin, *Magn. Reson. Med.*, 1999, **41**, 657.
24. M.von Kienlin, M. Beer, A. Greiser, D. Hahn, K. Harre, H. Kostler, W. Landschutz, T. Pabst, J. Sandstede, and S. Neubauer, *J. Magn. Reson. Imaging*, 2001, **13**, 521.
25. M. Beer, T. Seyfarth, J. Sandstede, W. Landschutz, C. Lipke, H. Kostler, M.von Kienlin, K. Harre, D. Hahn, and S. Neubauer, *J. Am. Coll. Cardiol.*, 2002, **40**, 1267.
26. O. Geier, A. M. Weng, A. Toepell, D. Hahn, M. Spindler, M. Beer, and H. Köstler, *Z. Med. Phys.*, 2013, **49**, 1.
27. M. Lustig, D. Donoho, and J. M. Pauly, *Magn. Reson. Med.*, 2007, **58**, 1182.
28. Y. Zhang, R. E. Gabr, J. Zhou, R. G. Weiss, and P. A. Bottomley, *J. Magn. Reson.*, 2013, **237**, 125.
29. K. P. Pruessmann, M. Weiger, M. B. Scheidegger, and P. Boesiger, *Magn. Reson. Med.*, 1999, **42**, 952.
30. R. A. Horn and C. R. Johnson, Matrix Analysis, Cambridge University Press: New York, 1990.
31. H. R. Brooker, T. H. Mareci, and J. Mao, *Magn. Reson. Med.*, 1987, **5**, 417.
32. M. A. Conway, P. A. Bottomley, R. Ouwerkerk, G. K. Radda, and B. Rajagopalan, *Circulation*, 1998, **97**, 1716.
33. P. A. Bottomley, in Encyclopedia of Magnetic Resonance, eds R. K. Harris and R. E. Wasylishen, John Wiley & Sons, Ltd: Chichester, 2009.
34. R. E. Gabr, R. Ouwerkerk, and P. A. Bottomley, *J. Magn. Reson.*, 2006, **179**, 152.
35. K. P. Pruessmann, M. Weiger, P. Börnert, and P. Boesiger, *Magn. Reson. Med.*, 2001, **46**, 638.
36. U. Dydak, M. Weiger, K. P. Pruessmann, D. Meier, and P. Boesiger, *Magn. Reson. Med.*, 2001, **46**, 713.
37. C. F. V. Loan, *J. Comput. Appl. Math.*, 2000, **123**, 85.
38. W. S. Hoge, D. H. Brooks, B. Madore, and W. E. Kyriakos, *Concepts Magn. Reson. Part A*, 2005, **27**, 17.
39. J. R. Roebuck, D. O. Hearshen, M. O'Donnell, and T. Raidy, *Magn. Reson. Med.*, 1993, **30**, 277.
40. A. Simonetti, W. Melssen, M. Van der Graaf, A. Heerschap, and L. Buydens, *J. Magn. Reson.*, 2002, **159**, 151.
41. H. Zhu, R. Ouwerkerk, and P. B. Barker, *Magn. Reson. Med.*, 2010, **63**, 1486.